A Distribution Independent Ship Detector for PolSAR Images

Zhou Xu , Chongyi Fan , Shuiying Cheng, Jian Wang, and Xiaotao Huang, *Senior Member, IEEE*

Abstract—Ship detection with polarimetric synthetic aperture radar (PolSAR) images has attracted a lot of attention in recent years. However, modeling the distribution of clutter is a complicated task. This article introduces a distribution independent ship detector for PolSAR images. First, in order to improve the detection performance, the multichannel PolSAR data are projected onto a 1-D space utilizing an adaptive linear filter. The design of linear filter is modeled as a nonconvex optimization problem with the principle of maximization target-to-clutter ratio, which is solved by an iteration optimization algorithm. Then, the convergence and computational complexities of the proposed algorithm are theoretically analyzed. After that, a distribution independent detector with a bounded constant false alarm rate property is proposed to distinguish ships from sea clutter. The detection threshold is calculated based on the Markov inequality without modeling the statistical distribution of clutter. Experiments are carried out on real Radarsat-2 and AirSAR data to test the proposed detector. The results demonstrate that the proposed detector, which takes the distribution independent and unsupervised properties as the main advantages, also achieves comparable detection performance with state-of-the-art methods. Moreover, additional experiments verify the robustness of the proposed detector to the initialization of the algorithm, even though the optimization problem is nonconvex. Finally, the effects on detection results caused by polarization characteristics are investigated to give a further explanation about linear polarization enhancement.

Index Terms—Bounded constant false alarm rate (CFAR), distribution independent detector, polarimetric synthetic aperture radar (PolSAR), ship detection, target-to-clutter ratio (TCR).

I. INTRODUCTION

DURING the past decades, polarimetric synthetic aperture radar (PolSAR) has played a significant role in many applications, such as marine surveillance and terrain classification. Compared with the single polarization synthetic aperture radar

Zhou Xu is with the College of Electronic Science and Engineering, National University of Defense Technology, Changsha 410073, China, and also with the College of Electronic Countermeasure, National University of Defense Technology, Hefei 230037, China (e-mail: zhouzhou900521@126.com).
Chongyi Fan, Jian Wang, and Xiaotao Huang are with the College of Electronic Science and Engineering, National University of Defense Technology, Changsha 410073, China (e-mail: chongyifan@nudt.edu.cn; hurri_can@163.com; xiaotaohuang@nudt.edu.cn).
Shuiying Cheng is with the College of Electronic Countermeasure, National University of Defense Technology, Hefei 230037, China (e-mail: csyebox@163.com).

(SAR), in which only the intensity and texture features can be utilized [1], [2], PolSAR provides polarization characteristics of the observation scenario, making it possible to distinguish targets of interest in polarization domain [3]–[5]. Consequently, PolSAR shows stronger abilities on target detection and recognition than its single polarization counterpart. Among a variety of different applications, ship detection has been widely studied for many years and several achievements have been achieved [6]–[9].

In most cases, polarimetric detectors project the multichannel PolSAR data onto a 1-D polarization feature domain to distinguish targets from clutter first [8], [10]–[21]. After that, detection procedure is carried out on this domain. Among the ship detection methods, constant false alarm rate (CFAR) detector, trying to keep the probability of false alarm constant, is the most popular one [19], [20], [22]–[30], in which the pixels that are significantly different from clutter are regarded as targets. Therefore, the following two critical problems have to be addressed when designing a PolSAR CFAR detector.

The first one is to extract an appropriate polarization feature. To address this problem, considerable detectors have been proposed, including polarimetric SPAN (total power), power maximization synthesis [10], and polarimetric matched filter [11], to name a few. Additionally, polarization scattering mechanism provides another important way to extract polarization features. Cameron *et al.* proposed the coherent decomposition method [12], and Ringrose and Harris applied it to ship detection [14]. Recently, based on perturbation analysis of the target space, Marino *et al.* proposed a detector called the geometrical perturbation-polarimetric notch filter (GP-PNF), showing pleasant performance on ship detection [15], [16]. Inspired by GP-PNF, an ambiguity removal polarimetric notch filter is proposed in [18] to remove azimuth ambiguities and detect ships simultaneously. Lin *et al.* [19] suggested to adopt the generalized polarization relative entropy to measure the differences between ships and sea clutter in scattering mechanism. The similar pixel number feature was used in [21] to deal with ship detection under the low and medium sea conditions. Studies in [4] also show that the man-made targets perform differently from the natural ones in reflection nonstationarity and asymmetry properties. Apart from this, some learning methods, such as sparse representation [31], [32], convolutional neural network [33], and support vector machine [34], are also introduced to ship detection or classification for PolSAR images. One of the most important criteria to evaluate the quality of polarization feature is the target-to-clutter ratio (TCR) [35], and a higher TCR usually brings benefits to

detection performance. However, in most situations, choosing an appropriate polarization feature is not always easy, since it requires heavy workload from experienced researchers. Moreover, the polarization feature also relies on a variety of factors, such as the type of targets and the frequency band of radar. Therefore, it is impossible to find a suitable polarization feature to describe all situations.

On the other hand, finding proper statistical models for clutter in the polarization feature domain is also important to determine the detection threshold. As radar resolution gets higher, the distribution of clutter appears non-Gaussian structure. For the GP-PNF detector, Fisher distribution has been used to model the nonhomogeneous sea clutter [20]. Chen *et al.* proposed to model the clutter with a generalized Laplacian distribution in the cross-entropy domain [25]. In [27], the PolSAR clutter data have been characterized by the K-Wishart distribution. Song *et al.* suggested that the sea clutter can be approximated by the mixture of Gaussian [30]. Although a set of distributions have been proposed, clutter modeling still suffers from poor adaptability and heavy computational complexity.

Generally, this article addresses the two problems mentioned earlier. For polarization feature extraction, a linear filter is used to project the multichannel PolSAR data onto a 1-D space, and the coefficients of filter are chosen adaptively aiming at maximizing the TCR. Then, we propose a distribution independent detector with bounded CFAR properties, i.e., the actually achieved probability of false alarm is always lower than the given one regardless of the clutter distribution. At last, the effectiveness of the proposed detector is verified by experiments on real PolSAR data. In particular, this article makes the following contributions.

1) *An optimization model for target enhancement:* In order to distinguish targets and clutter, the target enhancement process is modeled as an optimization problem with the goal of maximizing TCR.

2) *An efficient algorithm to solve the target enhancement optimization model:* We devise a cyclic algorithm to solve the nonconvex target enhancement optimization problem. Moreover, the convergence and computational complexities of the proposed algorithm are theoretically analyzed. Meanwhile, we also show the robustness of the proposed algorithm to its initialization, which will facilitate its further usage.

3) *A distribution independent detector with bounded CFAR property:* Based on the Markov inequality, a distribution independent detector with bounded CFAR properties is proposed. Different from conventional CFAR detectors, only the statistical moments are needed for the proposed detector when calculating threshold. Thus, it is distribution independent.

The remainder of this article is organized as follows. We briefly introduce the polarization data model and formulate the target detection problem in Section II. In Section III, the proposed novel detector is presented. In particular, the target enhancement optimization model and the detection criterion are provided. Section IV presents the optimization algorithm for target enhancement, including the analyses of convergence and computational complexities. Numerical experiments on real Radarsat-2 and AirSAR data are presented in Section V. Finally, we conclude the whole article in Section VI.

II. POLARIZATION DATA AND PROBLEM FORMULATION

A. Polarization Data

For a fully PolSAR system, the complex scattering matrix (Sinclair matrix) is given by [3]

$$\boldsymbol{S} = \begin{bmatrix} S_{\text{HH}} & S_{\text{HV}} \\ S_{\text{VH}} & S_{\text{VV}} \end{bmatrix} \tag{1}$$

where S_{HV} is the complex scattering coefficient with transmitting vertical polarization and receiving horizontal polarization, and the others are defined similarly. In order to analyze distributed targets, the polarization coherence matrix $\boldsymbol{T}$ and the polarization covariance matrix $\boldsymbol{C}$ are used, given by [36]

$$\begin{cases} \boldsymbol{T} = \text{E}[\boldsymbol{k}\boldsymbol{k}^{\text{H}}] \\ \boldsymbol{C} = \text{E}[\boldsymbol{\Omega}\boldsymbol{\Omega}^{\text{H}}] \end{cases} \tag{2}$$

where $\boldsymbol{k} = \frac{1}{\sqrt{2}}[S_{\text{HH}} + S_{\text{VV}}, S_{\text{HH}} - S_{\text{VV}}, 2S_{\text{HV}}]^{\text{T}}$ is the Pauli vector, $\boldsymbol{\Omega} = [S_{\text{HH}}, \sqrt{2}S_{\text{HV}}, S_{\text{VV}}]^{\text{T}}$ is the Lexicographic vector, and E[·] denotes the statistical expectation. The superscript T and H denote transpose and conjugate transpose, respectively. Besides, other polarization characteristics can be also extracted to describe the targets of interest, after some algebraic manipulations on $\boldsymbol{S}$, $\boldsymbol{T}$, and $\boldsymbol{C}$ [12]–[14], [37].

B. Problem Formulation

Suppose that $\boldsymbol{v} \in \mathbb{C}^{D \times 1}$ is the vectorization of some certain polarization characteristics, which may be the coherence matrix, covariance matrix, or any kinds of characteristics.

The target detection problem in clutter can be formulated as the binary hypothesis testing [38]

$$\begin{cases} \mathcal{H}_0 : \boldsymbol{v} = \boldsymbol{s} + \boldsymbol{n} \\ \mathcal{H}_1 : \boldsymbol{v} = \boldsymbol{c} + \boldsymbol{n} \end{cases} \tag{3}$$

where $\boldsymbol{n}$ is the system noise vector, $\boldsymbol{s}$ and $\boldsymbol{c}$ denote the polarization characteristic vector of target and clutter, respectively. Denote $\boldsymbol{c}_0$ by the statistical expectation of $\boldsymbol{c}$, then (3) is equivalent to the following hypothesis testing:

$$\begin{cases} \mathcal{H}_0 : \boldsymbol{x} = \boldsymbol{s} - \boldsymbol{c}_0 + \boldsymbol{n} \\ \mathcal{H}_1 : \boldsymbol{x} = \boldsymbol{c} - \boldsymbol{c}_0 + \boldsymbol{n} \end{cases} \tag{4}$$

where $\boldsymbol{c}_0 = \text{E}[\boldsymbol{c}]$ and $\boldsymbol{x} = \boldsymbol{v} - \boldsymbol{c}_0$.

Our purpose is to design an appropriate normalized filter $\boldsymbol{w} \in \mathbb{C}^{D \times 1}$, which projects $\boldsymbol{x}$ onto a 1-D space as follow: $g = \boldsymbol{w}^{\text{H}}\boldsymbol{x}$. Then, we consider the traditional square law detector

$$|g|^2 \underset{\mathcal{H}_1}{\overset{\mathcal{H}_0}{\gtrless}} T \tag{5}$$

where T is the detection threshold.

Assume that $\boldsymbol{c} \sim \mathcal{CN}(\boldsymbol{c}_0, \boldsymbol{R}_c)$ and $\boldsymbol{n} \sim \mathcal{CN}(0, \sigma^2 \mathbf{I})$ are independent complex Gaussian variables. Under this assumption, detection probability P_d and probability of false alarm P_{fa} can

be written as [39]

$$P_d = \Pr\left\{ \chi_{\mathrm{nc}}^2\left(|g|^2; 2, \boldsymbol{w}^{\mathrm{H}}\left(\boldsymbol{s} - \boldsymbol{c}_0\right)\left(\boldsymbol{s} - \boldsymbol{c}_0\right)^{\mathrm{H}}\boldsymbol{w}, \tfrac{\sigma^2}{2}\right) \geq T \right\}$$
$$P_{\mathrm{fa}} = \Pr\left\{ \mathrm{Exp}\left(|g|^2; \boldsymbol{w}^{\mathrm{H}}\left(\boldsymbol{R}_c + \sigma^2\mathbf{I}\right)\boldsymbol{w}\right) \geq T \right\}$$

$$(6)$$

where $\chi_{\mathrm{nc}}^2(y; a, b, c)$ denotes the noncentral chi-square distribution with a degrees of freedom and parameters b, c; $\mathrm{Exp}(y; a)$ denotes the exponential distribution with parameter a.

It is clearly observed from (6) that for the given σ^2 and T, P_d monotonically increases with respect to $\boldsymbol{w}^{\mathrm{H}}(\boldsymbol{s} - \boldsymbol{c}_0)(\boldsymbol{s} - \boldsymbol{c}_0)^{\mathrm{H}}\boldsymbol{w}$, which can be regarded as the distance between targets and the mean of clutter in the projected space. Meanwhile, P_{fa} monotonically decreases with respect to $\boldsymbol{w}^{\mathrm{H}}(\boldsymbol{R}_c + \sigma^2\mathbf{I})\boldsymbol{w}$, which can be regarded as the spread of clutter in the projected space. However, sea clutter is non-Gaussian in most cases and the detection performance can be hardly derived in a closed form. Nevertheless, we can also learn from (6) that large distance between targets and clutter brings benefit to detection probability, whereas small cluttering spreading reduces the probability of false alarm.

Based on the aforementioned discussion, we formulate the following optimization problem to design $\boldsymbol{w}$ as

$$\max_{\boldsymbol{w}} \frac{\boldsymbol{w}^{\mathrm{H}}\left(\boldsymbol{s} - \boldsymbol{c}_0\right)\left(\boldsymbol{s} - \boldsymbol{c}_0\right)^{\mathrm{H}}\boldsymbol{w}}{\boldsymbol{w}^{H}\left(\boldsymbol{R}_c + \sigma^2\mathbf{I}\right)\boldsymbol{w}}. \qquad (7)$$

Interestingly, the objective in (7) also represents the TCR when considering the hypothesis testing in (4). Thus, we know that the optimal filter $\boldsymbol{w}^*$ projects the multichannel polarization data onto a 1-D space, where the maximal TCR is achieved. However, one may observe from (7) that the optimal filter $\boldsymbol{w}^*$ relies on $(\boldsymbol{R}_c, \boldsymbol{c}_0, \boldsymbol{s})$, which should be estimated from the PolSAR data. In the following sections, we focus on solving the filter $\boldsymbol{w}^*$ and designing detectors based on (7).

III. Target Enhancement Optimization Model and Distribution Independent Detector

As mentioned earlier, the optimal filter $\boldsymbol{w}^*$ relies on $(\boldsymbol{R}_c, \boldsymbol{c}_0, \boldsymbol{s})$. Unfortunately, $(\boldsymbol{R}_c, \boldsymbol{c}_0, \boldsymbol{s})$ is unavailable, because we do not know whether a pixel belongs to targets or clutter in advance. In this section, we modify the optimization model in (7) slightly and propose a distribution independent detection scheme to meet practical situations.

A. Target Enhancement Optimization Model

Assume that $\boldsymbol{V} = [\boldsymbol{v}_1, \boldsymbol{v}_2, \boldsymbol{v}_3, \ldots, \boldsymbol{v}_N]$ is the polarization data matrix mixed with targets and clutter. Let Θ be the dataset consisting of targets, and Υ be the dataset consisting of clutter. $\mathbf{1}_N$ and $\mathbf{I}_N$ denote the row unitary vector and the corresponding identity matrix with size N, respectively. The target labels are defined by a binary indicator $\mathbf{1}^\Theta$, where the ith element $\mathbf{1}^\Theta(i) = 1$, if $\boldsymbol{v}_i \in \Theta$, otherwise $\mathbf{1}^\Theta(i) = 0$. The diagonal matrix formed by $\mathbf{1}^\Theta$ is defined as $\boldsymbol{I}^\Theta = \mathrm{diag}(\mathbf{1}^\Theta)$. While the clutter indicator $\mathbf{1}^\Upsilon(\mathbf{1}^\Upsilon = \mathbf{1}_N - \mathbf{1}^\Theta)$ and diagonal matrix $\boldsymbol{I}^\Upsilon(\boldsymbol{I}^\Upsilon = \mathbf{I}_N - \boldsymbol{I}^\Theta)$ are defined accordingly. We also define the target matrix $\boldsymbol{V}^\Theta$

and the clutter matrix $\boldsymbol{V}^\Upsilon$ as

$$\begin{cases} \boldsymbol{V}^\Theta = \boldsymbol{V}\boldsymbol{I}^\Theta \\ \boldsymbol{V}^\Upsilon = \boldsymbol{V}\boldsymbol{I}^\Upsilon = \boldsymbol{V}\left(\mathbf{I}_N - \boldsymbol{I}^\Theta\right) \end{cases}. \qquad (8)$$

Note that (7) is derived to enhance the single target $\boldsymbol{s}$. In fact, the polarization data $\boldsymbol{V}$ contain several targets, which constitute the target dataset Θ. In order to meet the practical situation and enhance targets from the statistical view, it is reasonable to use the expectation value $\boldsymbol{R}_s = \mathrm{E}[(\boldsymbol{s} - \boldsymbol{c}_0)(\boldsymbol{s} - \boldsymbol{c}_0)^{\mathrm{H}}]$ instead of $(\boldsymbol{s} - \boldsymbol{c}_0)(\boldsymbol{s} - \boldsymbol{c}_0)^{\mathrm{H}}$ in (7).

Nevertheless, the true value of $\boldsymbol{c}_0$, $\boldsymbol{R}_c$, or $\boldsymbol{R}_s$ is still unavailable, thus we have to use the estimated value instead. Combining (4) and (8), the estimators for $\boldsymbol{c}_0$, $\boldsymbol{R}_c$, and $\boldsymbol{R}_s$ are given by

$$\begin{cases} \hat{\boldsymbol{c}}_0 = \frac{\boldsymbol{V}\mathbf{1}^\Upsilon}{\mathrm{tr}(\boldsymbol{I}^\Upsilon)} \\ \hat{\boldsymbol{R}}_c = \frac{(\boldsymbol{V} - \hat{\boldsymbol{c}}_0\mathbf{1}_N^{\mathrm{T}})\boldsymbol{I}^\Upsilon(\boldsymbol{V} - \hat{\boldsymbol{c}}_0\mathbf{1}_N^{\mathrm{T}})^{\mathrm{H}}}{\mathrm{tr}(\boldsymbol{I}^\Upsilon)} - \sigma^2\mathbf{I} \\ \hat{\boldsymbol{R}}_s = \frac{(\boldsymbol{V} - \hat{\boldsymbol{c}}_0\mathbf{1}_N^{\mathrm{T}})\boldsymbol{I}^\Theta(\boldsymbol{V} - \hat{\boldsymbol{c}}_0\mathbf{1}_N^{\mathrm{T}})^{\mathrm{H}}}{\mathrm{tr}(\boldsymbol{I}^\Theta)} - \sigma^2\mathbf{I} \end{cases} \qquad (9)$$

where $\mathrm{tr}(\cdot)$ denotes the trace operation of a squared matrix.

To this end, we recast (7) with the estimated values in (9) as

$$\max_{\boldsymbol{w},\Theta} \frac{\boldsymbol{w}^{\mathrm{H}}\left(\mathrm{tr}(\boldsymbol{I}^\Upsilon)\boldsymbol{V}\boldsymbol{H}(\Theta)\boldsymbol{V}^{\mathrm{H}} - \sigma^2\mathbf{I}\right)\boldsymbol{w}}{\mathrm{tr}(\boldsymbol{I}^\Theta)\boldsymbol{w}^{\mathrm{H}}\boldsymbol{V}\boldsymbol{G}(\Theta)\boldsymbol{V}^{\mathrm{H}}\boldsymbol{w}} \qquad (10)$$

where

$$\boldsymbol{G}(\Theta) = \boldsymbol{I}^\Upsilon\left(\mathbf{I}_N - \frac{\mathbf{1}^\Upsilon(\mathbf{1}^\Upsilon)^{\mathrm{T}}}{\mathrm{tr}(\boldsymbol{I}^\Upsilon)}\right)\left(\mathbf{I}_N - \frac{\mathbf{1}^\Upsilon(\mathbf{1}^\Upsilon)^{\mathrm{T}}}{\mathrm{tr}(\boldsymbol{I}^\Upsilon)}\right)^{\mathrm{T}}\boldsymbol{I}^\Upsilon$$
$$\boldsymbol{H}(\Theta) = \boldsymbol{I}^\Theta\left(\mathbf{I}_N - \frac{\mathbf{1}^\Upsilon(\mathbf{1}^\Theta)^{\mathrm{T}}}{\mathrm{tr}(\boldsymbol{I}^\Upsilon)}\right)\left(\mathbf{I}_N - \frac{\mathbf{1}^\Upsilon(\mathbf{1}^\Theta)^{\mathrm{T}}}{\mathrm{tr}(\boldsymbol{I}^\Upsilon)}\right)^{\mathrm{T}}\boldsymbol{I}^\Theta.$$

$$(11)$$

It should be noted that (10) is unstable, since the matrix $\boldsymbol{V}\boldsymbol{G}(\Theta)\boldsymbol{V}^{\mathrm{H}}$ on the denominator is semidefinite, which means that there exists $\boldsymbol{w} \neq 0$ such that $\boldsymbol{w}^{\mathrm{H}}\boldsymbol{V}\boldsymbol{G}(\Theta)\boldsymbol{V}^{\mathrm{H}}\boldsymbol{w} = 0$. In order to get a stable model, a positive definite matrix on the denominator is needed. In practical situations, system noise power σ^2 is small enough compared with the clutter and target power. Therefore, the stability of (10) can be further enhanced by adding a relatively small term $\sigma^2\boldsymbol{w}^{\mathrm{H}}\boldsymbol{w}$ to the numerator and denominator, which will not significantly affects the model. For this reason, the following modified TCR enhancement optimization model is used:

$$\max_{\boldsymbol{w},\Theta}\mathrm{TCR}(\boldsymbol{w}, \mathbf{1}^\Theta) = \frac{\mathrm{tr}(\boldsymbol{I}^\Upsilon)\boldsymbol{w}^{\mathrm{H}}\boldsymbol{V}\boldsymbol{H}(\Theta)\boldsymbol{V}^{\mathrm{H}}\boldsymbol{w}}{\boldsymbol{w}^{\mathrm{H}}\left(\mathrm{tr}(\boldsymbol{I}^\Theta)\boldsymbol{V}\boldsymbol{G}(\Theta)\boldsymbol{V}^{\mathrm{H}} + \sigma^2\mathbf{I}\right)\boldsymbol{w}}. \qquad (12)$$

B. Distribution Independent Detector

Once the optimal filter $\boldsymbol{w}^*$ and $\hat{\Theta}$ were obtained from (12), we need to determine a threshold T to meet the given false alarm rate P_{fa}. Namely

$$\Pr\{\boldsymbol{w}^{\mathrm{H}}\boldsymbol{v}\boldsymbol{v}^{\mathrm{H}}\boldsymbol{w} \geq T; \mathcal{H}_1\} = P_{\mathrm{fa}}. \qquad (13)$$

Different from the assumptions in traditional detectors, we suppose that the clutter distribution of $\boldsymbol{w}^{\mathrm{H}}\boldsymbol{v}\boldsymbol{v}^{\mathrm{H}}\boldsymbol{w}$ is unknown, and determine T by finding the upper bound of P_{fa} based on the following lemma.
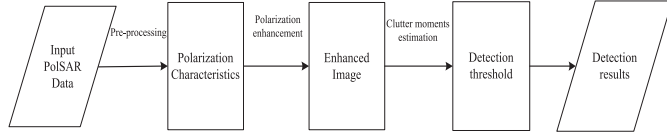
Fig. 1. Flowchart of the proposed detection procedure.

Lemma 1: (Markov inequality) Let X be a nonnegative random variable, for any $r > 0$ and $x > 0$, then

$$\Pr\{X \ge x\} \le \frac{\mathrm{E}\left[X^r\right]}{x^r}.$$

Proof: Proof can be found in [40] and references therein. ∎

It should be pointed out that $\boldsymbol{w}^{\mathrm{H}}\boldsymbol{v}\boldsymbol{v}^{\mathrm{H}}\boldsymbol{w} \ge 0$ holds for any $\boldsymbol{w}$ and $\boldsymbol{v}$. As an immediate consequence of *Lemma 1*, we get the following inequality:

$$\Pr\{X \ge x\} \le P_{\mathrm{fa}} \tag{14}$$

if

$$P_{\mathrm{fa}} \ge \min\left\{\frac{\mathrm{E}\left[X\right]}{x}, \ldots, \frac{\mathrm{E}\left[X^r\right]}{x^r}\right\}. \tag{15}$$

Let $m_r = \mathrm{E}_{\hat{\Upsilon}}[(\boldsymbol{w}^{\mathrm{H}}\boldsymbol{v}\boldsymbol{v}^{\mathrm{H}}\boldsymbol{w})^r]$ be the estimated statistical moments of order r for $\boldsymbol{w}^{\mathrm{H}}\boldsymbol{v}\boldsymbol{v}^{\mathrm{H}}\boldsymbol{w}$. For a given P_{fa}, the threshold can be chosen as

$$T = \min\{m/P_{\mathrm{fa}}, \sqrt{m_2/P_{\mathrm{fa}}}, \ldots, \sqrt[r]{m_r/P_{\mathrm{fa}}}\}. \tag{16}$$

Therefore, the false alarm rate will be bounded by P_{fa} without modeling the distribution of clutter. The flowchart of the detection procedure is shown in Fig. 1 to make the proposed detector easy to understand.

IV. OPTIMIZATION ALGORITHMS

In this section, we devise a cyclic optimization algorithm to solve the problem in (12). Specifically, we initialize the indicator $\mathbf{1}_0^{\Theta}$, then alternatively maximize the objective with respect to $\boldsymbol{w}_t$ for a fixed $\mathbf{1}_t^{\Theta}$ and maximize the objective with respect to the $\mathbf{1}_{t+1}^{\Theta}$ for a fixed $\boldsymbol{w}_t$ at each iteration. Finally, we prove the convergence of the proposed optimization algorithm. Note that the maximization problem in (12) is equivalent to

$$Q = \max_{\Theta} \lambda_{\max}\left(\mathrm{tr}(\boldsymbol{I}^{\Upsilon})\left(\mathrm{tr}(\boldsymbol{I}^{\Theta})\boldsymbol{V}\boldsymbol{G}(\Theta)\boldsymbol{V}^{\mathrm{H}}\right.\right.$$
$$\left.\left. + \sigma^2\boldsymbol{I}\right)^{-1}\boldsymbol{V}\boldsymbol{H}(\Theta)\boldsymbol{V}^{\mathrm{H}}\right) \tag{17}$$

where $\lambda_{\max}(\boldsymbol{A})$ denotes the maximal eigenvalue of $\boldsymbol{A}$, meaning that the maximum of objective in (12) is independent from $\boldsymbol{w}$. But (17) is a nonlinear binary optimization problem, which is also a nonpolynomial hard problem [41], [42] and cannot be well solved in polynomial time. Next, we introduce the alternative maximization scheme to solve (12), which consists of two steps: filter updating and indicator updating.

A. Filter Updating

Note that $\mathrm{tr}(\boldsymbol{I}^{\Theta})\boldsymbol{V}\boldsymbol{G}(\Theta)\boldsymbol{V}^{\mathrm{H}} + \sigma^2\boldsymbol{I}$ is Hermitian positive definite and $\boldsymbol{V}\boldsymbol{H}(\Theta)\boldsymbol{V}^{\mathrm{H}}$ is Hermitian semidefinite. Substitute

TABLE I
OPTIMIZATION ALGORITHMS FOR TARGET ENHANCEMENT

Input: Polarization Data $\boldsymbol{V}$, noise power σ^2 and tolerable error ε.
Output: Optimal filter $\boldsymbol{w}^*$ and target indicator $\mathbf{1}_*^{\Theta}$.
Initialization:
Set $t = 0$, initialize the indicator vector $\mathbf{1}_0^{\Theta}$.
Iteration:
Step 1: compute $\boldsymbol{w}_t$ with (18);
Step 2: *loop*: $i = 1 : N$
compute $\mathbf{1}_t^{\Theta,i}$ with (19) and update $\mathbf{1}_{t+1}^{\Theta}(i)$ with (20);
end loop.
Step 3: compute $\boldsymbol{w}_{t+1}$ with (18);
Step 4: calculate $\mathrm{TCR}^{(t)}$ and $\mathrm{TCR}^{(t+1)}$; let $t = t + 1$, repeat
step 1, step 2, step 3, step 4 until $\left(\mathrm{TCR}^{(t+1)} - \mathrm{TCR}^{(t)}\right)$
$/\mathrm{TCR}^{(t)} \le \varepsilon$.
Output: $\boldsymbol{w}^* = \boldsymbol{w}_{t+1}$, $\mathbf{1}_*^{\Theta} = \mathbf{1}_{t+1}^{\Theta}$.

$\mathbf{1}_t^{\Theta}$ for $\mathbf{1}^{\Theta}$ in (12), then the optimal filter $\boldsymbol{w}_t$ at the tth step can be represented by

$$\boldsymbol{w}_t = \mathcal{P}\left(\mathrm{tr}(\boldsymbol{I}^{\Upsilon})\left(\mathrm{tr}(\boldsymbol{I}^{\Theta})\boldsymbol{V}\boldsymbol{G}(\Theta)\boldsymbol{V}^{\mathrm{H}} + \sigma^2\boldsymbol{I}\right)^{-1}\boldsymbol{V}\boldsymbol{H}(\Theta)\boldsymbol{V}^{\mathrm{H}}\right) \tag{18}$$

where $\mathcal{P}(\boldsymbol{A})$ denotes the normalized principal eigenvector of $\boldsymbol{A}$.

B. Indicator Updating

Before the updating process, let us introduce the initialization of $\mathbf{1}_0^{\Theta}$. Apparently, the problem described in (12) is nonconvex, and the optimal solution depends on the initialization. In our work, the heuristic method is used to initialize $\mathbf{1}_0^{\Theta}$. More precisely, we initialize $\mathbf{1}_0^{\Theta}$ with the result obtained from a SPAN detector.

Now, let us turn to indicator updating schemes. Denote $\boldsymbol{w}_t$ and $\mathbf{1}_t^{\Theta}$ by the filter and indicator at the tth step of iteration, respectively. We adopt a perturbation method to get $\mathbf{1}_{t+1}^{\Theta}$ [43], [44] given that the elements in $\mathbf{1}_t^{\Theta}$ is 0 or 1. In detail, we perturb the ith element in $\mathbf{1}_t^{\Theta}$ by changing its class label, which can be represented as

$$\mathbf{1}_t^{\Theta,i} = \left|\left(\mathbf{1}_t^{\Theta} - \boldsymbol{e}_i\right)\right| \tag{19}$$

where $\boldsymbol{e}_i$ is the unit basis vector in the Euclidean space with the ith element to be 1, and $|\cdot|$ denotes the absolute value operation on each element.

The updating rule of indicator at the $(t+1)$th step is given by

$$\mathbf{1}_{t+1}^{\Theta}(i) = \begin{cases} \mathbf{1}_t^{\Theta}(i) & \mathrm{TCR}(\boldsymbol{w}_t, \mathbf{1}_t^{\Theta}) \ge \mathrm{TCR}(\boldsymbol{w}_t, \mathbf{1}_t^{\Theta,i}) \\ \left|\left(\mathbf{1}_t^{\Theta}(i) - 1\right)\right| & \text{otherwise} \end{cases}. \tag{20}$$

In order to give a clear expression, the optimization algorithm for solving (12) is summarized in Table I.

C. Further Discussions

In this section, we analyze the convergence as well as the computational complexities of the proposed algorithm.

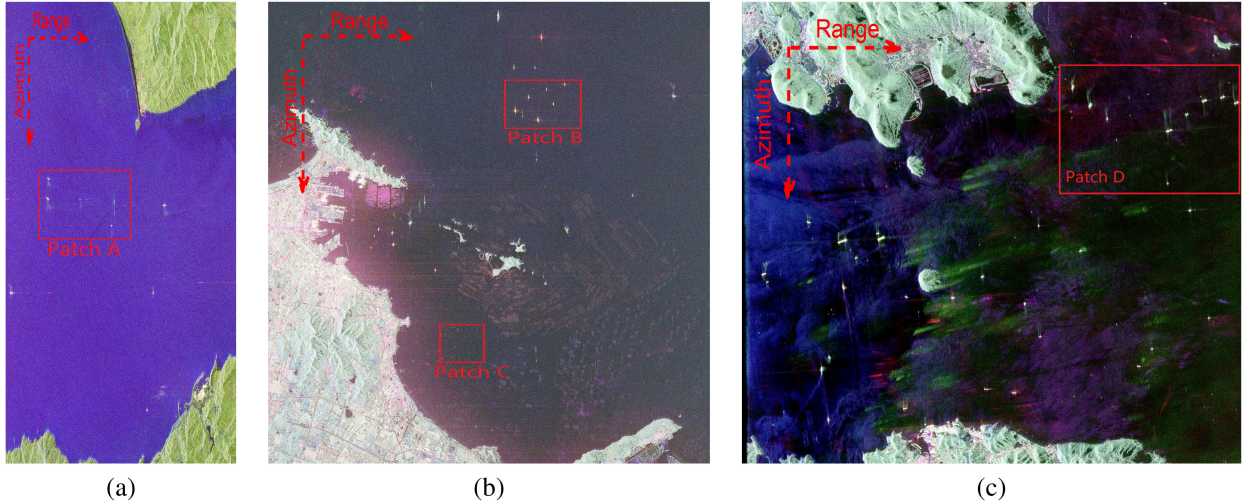*Proposition 1:* The algorithm presented in Table I converges to a stationary point.

Fig. 2. Pauli pseudocolored images. (a) Strait of Gibraltar. (b) Yantai port. (c) Kojima-wan.

TABLE II
EXPERIMENTAL DATA INFORMATION

	Scene 1	Scene 2	Scene 3
Sensor	Radarsat-2	Radarsat-2	AirSAR
Area	Gibraltar	Yantai Port	Kojima-wan
Date	2008.03.01	2015.06.02	2000.10.4
Frequency band	C	C	L
Azimuth looks	1	1	9
Range looks	1	1	1
Incident angle(°)	20.8-22.8	45.2-46.5	27.5-62.6
Sampled Resolution(m)	4.7×5.3	4.7×4.9	3.3×4.6
Wind speed(m/s)	Unknown	7-9	Unknown

Proof: Note that

$$\mathrm{TCR}(\boldsymbol{w}_t, \mathbf{1}_t^\Theta) \leq \mathrm{TCR}(\boldsymbol{w}_t, \mathbf{1}_{t+1}^\Theta) \leq \mathrm{TCR}(\boldsymbol{w}_{t+1}, \mathbf{1}_{t+1}^\Theta). \tag{21}$$

In (21), the first inequality holds due to the condition of perturbation described in (20), whereas the second inequality holds because $\boldsymbol{w}_{t+1}$ is optimized from (18).

On the other hand, for any t, the following inequality always holds:

$$\mathrm{TCR}(\boldsymbol{w}_t, \mathbf{1}_t^\Theta) \leq Q. \tag{22}$$

Obviously, Q is bounded for the sake that Θ is a finite set. Thus, $\mathrm{TCR}(\boldsymbol{w}_t, \mathbf{1}_t^\Theta)$ forms a monotonically increasing sequence with upper bounds. Consequently, the algorithm will converge to a stationary point. ∎

The computational complexities are proportional to the number of iterations. At each iteration, it involves $O(D^3)$ operations to calculate $\boldsymbol{w}_t$ and $O(N)$ operations to update $\mathbf{1}_t^\Theta$. Therefore, the total computational complexities of the proposed algorithm are $O(M(D^3 + N))$ with M being the number of iterations.

V. EXPERIMENTAL ANALYSIS

In this section, some experimental results and comparisons are provided to show the effectiveness of the proposed algorithm and detector.
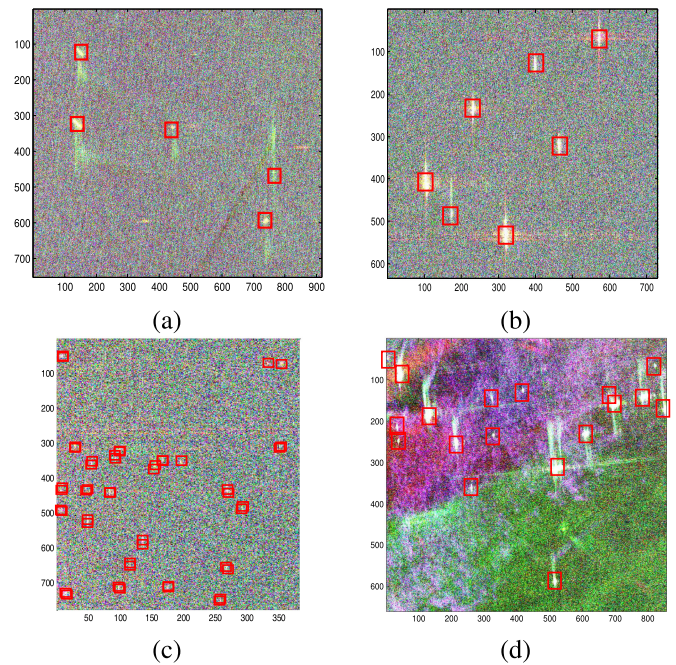

Fig. 3. Pauli colored images for each patch. (a) Patch A. (b) Patch B. (c) Patch C. (d) Patch D.

A. Experimental Data

The experimental data are selected from three large quad-polarization scenes, whose key information is illustrated in Table II. Four patches comprising ships and sea areas are extracted from these scenes, Fig. 2 shows the Pauli pseudocolored images of the original data, where the four experimental patches are marked in red rectangles. Moreover, Fig. 3 presents the corresponding Pauli pseudocolored images for each patch, where the ground truth data are manually labeled with red rectangles. The detailed information for each patch is illustrated in Table III.

Generally, these four patches represent three different cases for ship detection. The first case consists of Patches A and

TABLE III
DETAILED INFORMATION FOR EACH PATCH

Patch	Size(pixel)	Number of targets
Patch A	751×916	5
Patch B	633×729	7
Patch C	777×328	25
Patch D	659×855	18

Fig. 4. TCR curve versus number of iterations.

Fig. 5. Enhanced images for each patch (in decibel). (a) Patch A. (b) Patch B. (c) Patch C. (d) Patch D.
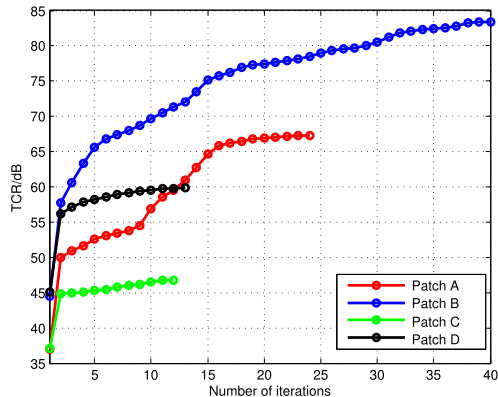
B, where scattering intensity of ships is strong enough compared with sea clutter. Patch C is the second case, for which the scattering intensity of ships is relatively weak compared with sea clutter. The third case is Patch D, where both strong and weak ships exist in the patch, and the sea clutter is also nonhomogeneous. From this point of view, the detection task over Patches C and D seems to be harder than that over Patches A and B.

The following numerical experiments are analyzed with MAT-LAB 2014a and performed in a standard PC (with CPU Core i5 3.0 GHz and 16-GB RAM).

B. Ship Detection and Comparisons

In this section, we explore the ship detection performance of our proposed detector and compare it with some current methods.

In the following experiments, unless otherwise specified, the polarization characteristic vector v is constructed by vectorizing the coherence matrix T. The noise power σ^2 is set to be 10^{-6} and ε is set to be 0.01. Additionally, the indicator vector $\mathbf{1}_0^\Theta$ is initialized by a SPAN detector where the clutter is modeled as Gama distribution, and false alarm rate P_{fa} is set to be 10^{-4}. Moreover, for the detection results given in the following, the missed alarms and false alarms are marked with yellow and blue ellipses, respectively.

The target enhancement procedure is implemented first. Fig. 4 depicts the TCR curve versus the number of iterations. As expected, the TCR monotonically increases and converges within several iterations. One can observe from the figure that Patch B achieves the highest TCR about 84 dB, meanwhile the TCR of Patch C is the lowest one (about 47 dB), which is consistent with the original data. Apart from this, the number of iterations varies among different patches. More precisely, the numbers of iterations for Patches A, B, C, and D are 24, 40, 12, and
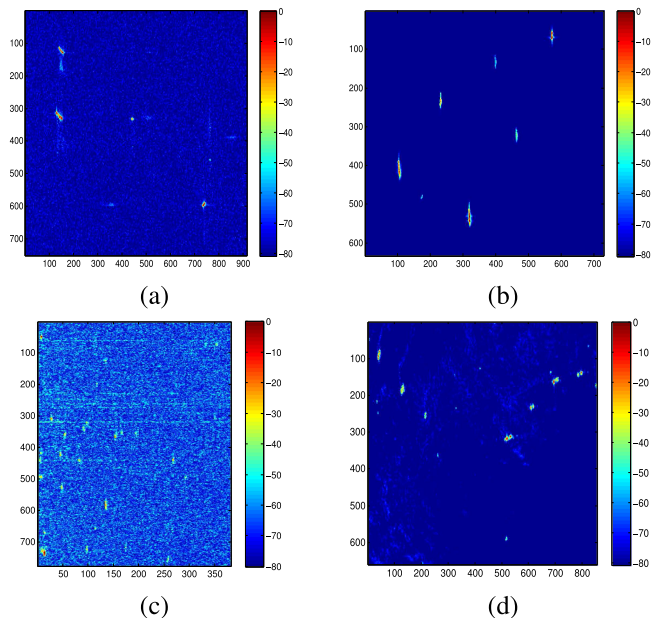
13, respectively. These results indicate that the procedure of target enhancement is adaptive and the final enhanced results rely on the original data. Fig. 5 illustrates the enhancement images of these four patches. Obviously, the targets are significantly enhanced and the clutter is well suppressed compared with the original data.

To this end, we begin the detection procedure with the first- and second-order statistical moments of clutter being used to estimate the threshold. Next, we study the principle of setting the upper bound of P_{fa} in our detector. Taking Patches A and C for example, Fig. 6 shows the corresponding detection results associated with different upper bounds of P_{fa}. It is easy to find that among the studied three parameters, namely, 10^{-2}, 10^{-3}, and 10^{-4}, 10^{-4} achieves the best performance for Patch A, since all the targets are detected and no false alarm occurs. Meanwhile, 10^{-2} seems to be the best one for Patch C due to the reason that it achieves the highest detection probability and only one false alarm occurs. This result shows that the balance between missed alarms and false alarms should be taken into consideration when setting the upper bound of P_{fa}. Therefore, it is better to use a low P_{fa} to control the false alarm rate for the image with high TCR, and a high P_{fa} to ensure the detection probability for the image with low TCR.

Following the guideline, detection experiments are carried out over the four patches and the corresponding detection results are illustrated in Fig. 7. As to the upper bounds of P_{fa}, they are set to be 10^{-4}, 10^{-5}, 5×10^{-2}, and 10^{-3} for Patches A, B, C, and D, respectively. We can see from the figure that all the ships in Patches A and B are well detected. However, several missed alarms as well as false alarms occur in Patch C due to the relatively low TCR. For Patch D, the detection results are acceptable given that 17 out of 18 ships are detected without
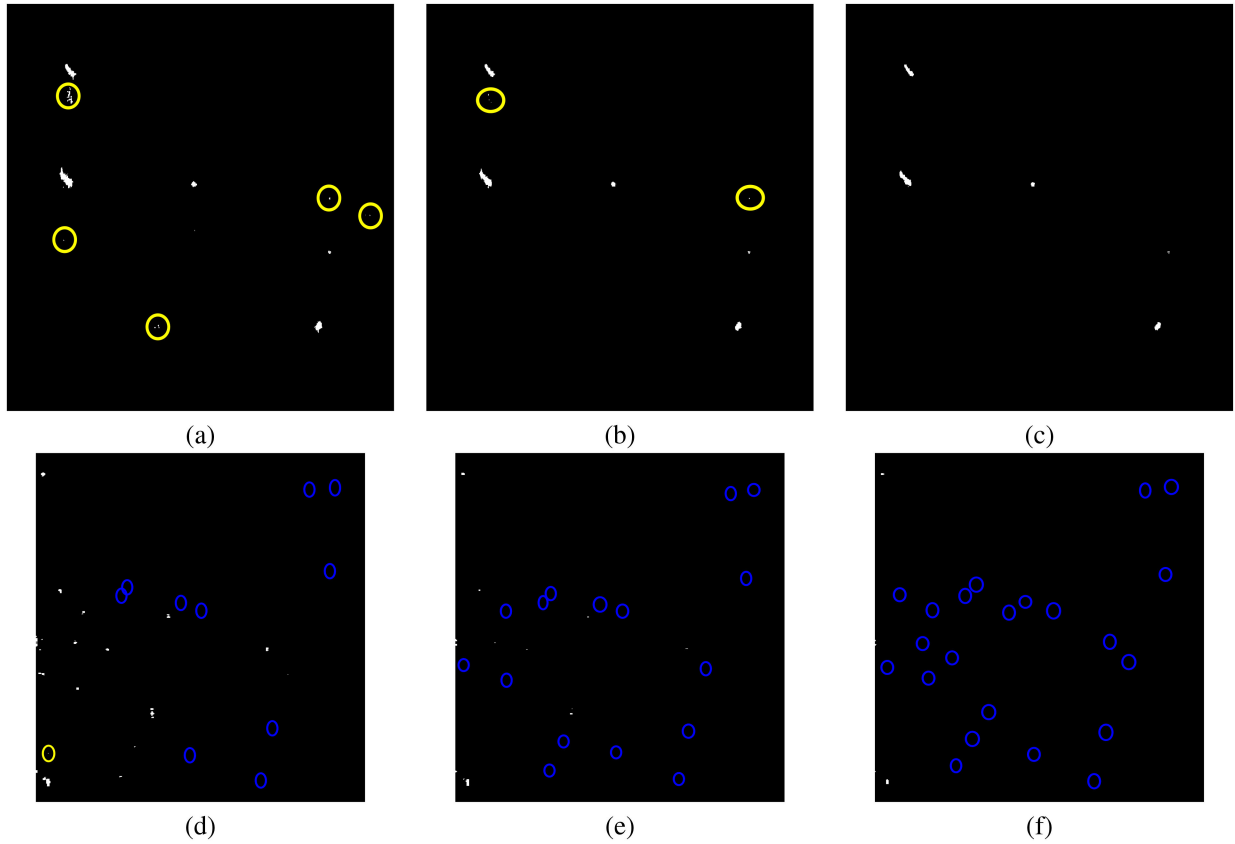
Fig. 6. Detection results with respect to different upper bounds of P_{fa}. (a) Patch A with $P_{\text{fa}} = 10^{-2}$. (b) Patch A with $P_{\text{fa}} = 10^{-3}$. (c) Patch A with $P_{\text{fa}} = 10^{-4}$. (d) Patch C with $P_{\text{fa}} = 10^{-2}$. (e) Patch C with $P_{\text{fa}} = 10^{-3}$. Patch C with $P_{\text{fa}} = 10^{-4}$.
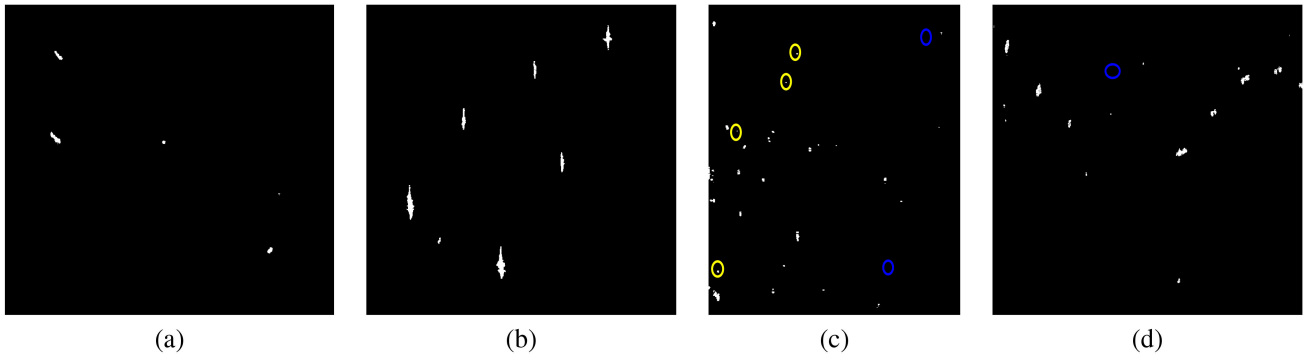

Fig. 7. Detection results with the proposed detector. (a) Patch A. (b) Patch B. (c) Patch C. (d) Patch D.

any false alarms. These results demonstrate that the proposed algorithm is suitable for ship detection in different cases.

Next, we compare the proposed detector with two current detection methods, namely, GP-PNF [20] and superpixel SM [31]. For the GP-PNF detector, P_{fa} is set to be 10^{-7}, 10^{-8}, 10^{-5}, and 10^{-5} for Patches A, B, C, and D, respectively. As to the superpixel SM detector, the superpixel scale is set to be 40 and thresholds are set manually in order to achieve the best detection performance, because thresholds are set empirically and no principle of setting threshold is given in [31]. Figs. 8 and 9 depict the detection results using GP-PNF and superpixel SM detector, respectively, where the training data region is marked with green rectangle in each patch.

In order to give a quantitative analysis of different detectors, the figure of merit (FoM) and the detection rate P_r are used to evaluate the detection performance, which are defined as follows [17]:

$$\text{FoM} = \frac{N_d}{N_g}, P_r = \frac{N_d}{N_g + N_f} \quad (23)$$

where N_d denotes the number of detected ships, N_g denotes the number of ground truth, and N_f is the number of false alarms.

Table IV exhibits comprehensive comparisons over the three detectors. It can be observed from the table that the superpixel SM slightly outperforms our detector, and achieves the best performance in terms of FoM and P_r. Nevertheless, the
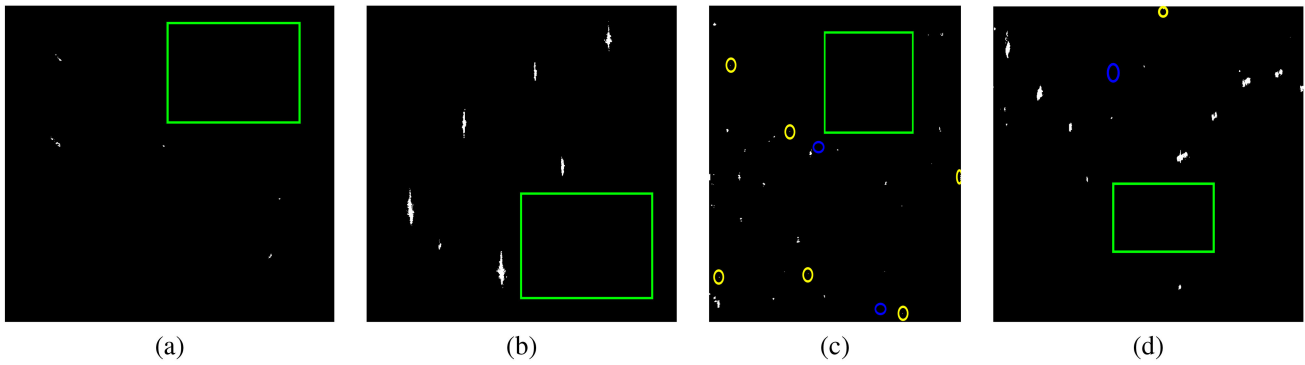
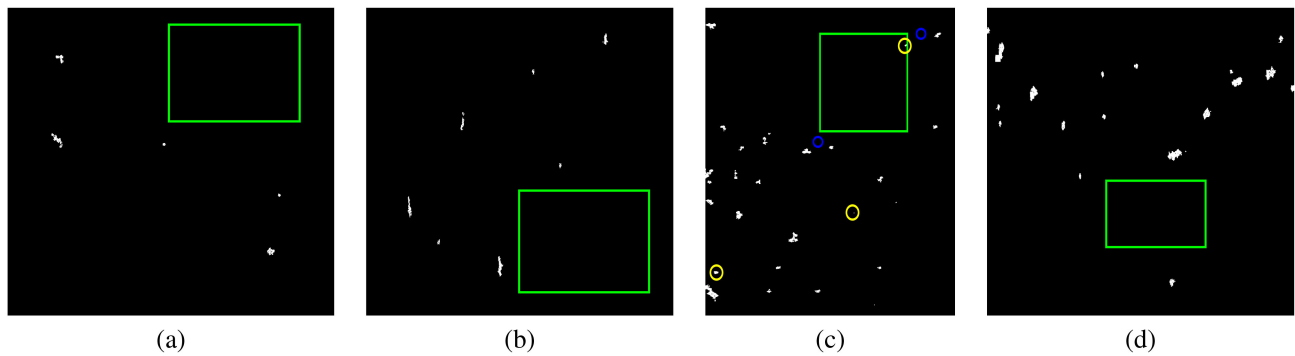Fig. 8. Detection results with the GP-PNF detector. (a) Patch A. (b) Patch B. (c) Patch C. (d) Patch D.

Fig. 9. Detection results with the superpixel SM detector. (a) Patch A. (b) Patch B. (c) Patch C. (d) Patch D.

TABLE IV
COMPARISONS FOR DIFFERENT DETECTORS

Detector	Training data	CFAR property	Clutter modeling	Patch	Running time/s		N_g	N_d	N_f	FoM	P_r
					Enhancement	Detection					
Proposed	Unnecessary	Bounded CFAR	Unnecessary	Patch A	6.2	0.002	5	5	0	1	1
				Patch B	6.9	0.005	7	7	0	1	1
				Patch C	1.3	0.001	25	23	4	0.92	0.79
				Patch D	2.8	0.003	18	17	0	0.94	0.94
				total	**17.2**	**0.011**	**55**	**52**	**4**	**0.95**	**0.88**
GP-PNF	Necessary	Yes	Necessary	Patch A	1.2	0.16	5	5	0	1	1
				Patch B	0.8	0.12	7	7	0	1	1
				Patch C	0.5	0.10	25	23	6	0.92	0.74
				Patch D	0.9	0.08	18	17	2	0.94	0.85
				total	**3.4**	**0.46**	**55**	**52**	**8**	**0.95**	**0.83**
Superpixel SM	Necessary	No	Unnecessary	Patch A	283.2	\	5	5	0	1	1
				Patch B	103.7	\	7	7	0	1	1
				Patch C	52.2	\	25	23	3	0.92	0.82
				Patch D	272.3	\	18	18	0	1	1
				total	**711.4**	\	**55**	**53**	**3**	**0.96**	**0.91**

Bold indicates the total running time.

performance of the three mentioned detectors is actually very similar, because they get the same FoM, and the maximal gap for different P_r is 0.08. From the perspective of computational complexities, the GP-PNF detector is the most efficient. Particularly, our detector is slower than the GP-PNF at the enhancement stage, since it involves solving a nonconvex optimization problem through iterations. The superpixel SM detector is extremely time consuming due to the superpixel segmentation and sparse representation processes, even though it achieves the best detection performance. On the other hand, at the detection stage, our detector is the fastest one, for the reason that only the statistical moments are needed to calculate the threshold. As

to the superpixel SM detector, the running time of detection is not illustrated given that thresholds are manually set. A careful inspection of the table reveals that the main advantages of our detector are the distribution independent and bounded CFAR properties, under the condition of getting similar detection performance. Compared with ours, the GP-PNF detector needs to model the distribution of clutter to ensure the CFAR property, whereas the superpixel SM detector cannot guarantee the CFAR property. Apart from this, training data are also necessary when utilizing the GP-PNF or superpixel SM detector, given the fact that GP-PNF detector needs the reference polarization feature of clutter to construct the GP-PNF characteristic, and superpixel
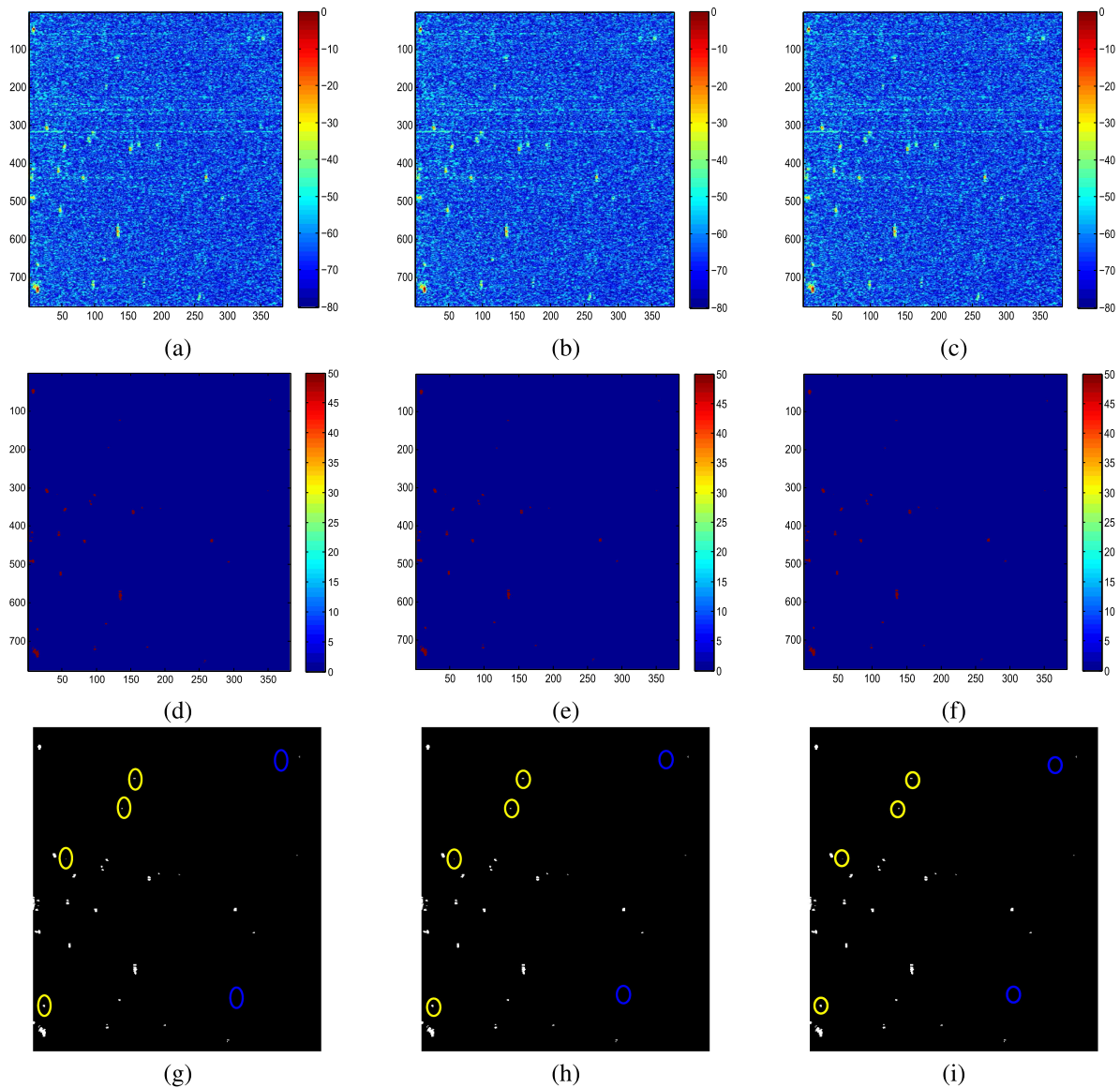
Fig. 10. Effects caused by different levels of noises for Patch C. (a) Average enhanced image with 10% pepper noise. (b) Average enhanced image with 20% pepper noise. (c) Average enhanced image with 50% pepper noise. (d) Accumulated detection image with 10% pepper noise. (e) Accumulated detection image with 20% pepper noise. (f) Accumulated detection image with 50% pepper noise. (g) Final detected image with 10% pepper noise. (h) Final detected image with 20% pepper noise. (i) Final detected image with 50% pepper noise.

SM detector needs the dictionary of clutter compute the residual of sparse representation. However, our detector can simultaneously enhance the target and estimate the clutter label, so no training data are needed for the proposed detector.

At the end of this section, it is worth pointing out that compared with the conventional CFAR detector, a relatively high P_{fa} is recommended for our detector (refer to the parameters setting for GP-PNF detector and our detector), especially for the images with low TCR, since P_{fa} used in our detector is the upper bound of the false alarm rate.

C. Effects of Initialization $\mathbf{1}_0^{\Theta}$

This section is devoted to the effects caused by perturbation of initialization $\mathbf{1}_0^{\Theta}$. As discussed earlier, the optimization problem described in (12) is nonconvex, thus the output enhanced image relies on the initial value $\mathbf{1}_0^{\Theta}$. Interestingly, as we will see in the sequel, the detection results are relatively robust to the perturbation of initialization, even though the optimization problem is nonconvex.

Considering the binary property of $\mathbf{1}_0^{\Theta}$, the pepper noises with different levels are used to corrupt the initial vector $\mathbf{1}_0^{\Theta}$. The experiments are carried out over Patches C and D.

All parameters are the same as the previous settings applied on our detector except 10%, 20%, and 50% level pepper noises are added to the initialization $\mathbf{1}_0^{\Theta}$ obtained from the SPAN detector. In order to eliminate the randomness caused by the random pepper noises, $M = 50$ Monte Carlo experiments are carried out and the statistical results are studied. Fig. 10 depicts the results obtained from Patch C. In particular, Fig. 10(a)–(c) plots
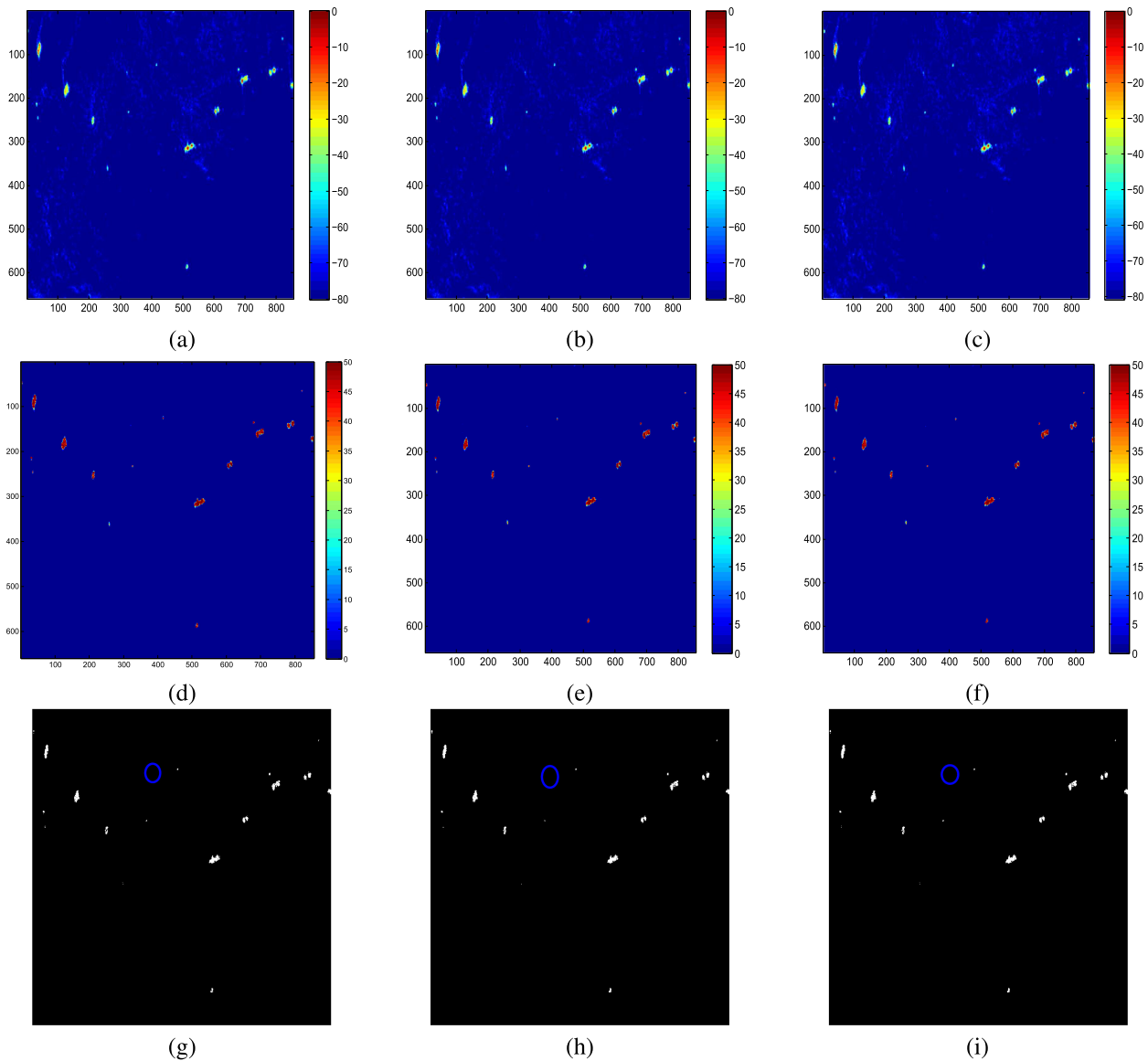
Fig. 11. Effects caused by different levels of noises for Patch D. (a) Average enhanced image with 10% pepper noise. (b) Average enhanced image with 20% pepper noise. (c) Average enhanced image with 50% pepper noise. (d) Accumulated detection image with 10% pepper noise. (e) Accumulated detection image with 20% pepper noise. (f) Accumulated detection image with 50% pepper noise. (g) Final detected image with 10% pepper noise. (h) Final detected image with 20% pepper noise. (i) Final detected image with 50% pepper noise.

the average enhanced image for the 50 Monte Carlo experiments under the three different levels of pepper noises. The corresponding accumulated detection images are shown in Fig. 10(d)–(f). Based on the accumulated images, we record the pixels that have been detected more than $0.8M$ times as targets and illustrate them in Fig. 10(g)–(i). We can observe from Fig. 10 that these enhanced images are similar to the one without pepper noise, and the final detection performance are the same with those without pepper noise in terms of FoM and P_r, even though 50% level pepper noise is added. Besides, Fig. 11 shows the corresponding results for Patch D, where similar phenomenon can be observed. Consequently, these results demonstrate the robustness of proposed detector to the perturbation of initialization.

D. Effects of Polarization Characteristic Vector

In this section, we investigate the effects caused by different polarization characteristics. Two additional experiments are carried out over Patch D, where two different polarization characteristics are used to enhance the image with other parameters being the same as the settings in Section V-B. Specifically, in the first experiment, we construct v by the eigenvalues of T, i.e., $v = [\lambda_1, \lambda_2, \lambda_3]^T$, where λ_i is the ith eigenvalue of T. While in the second experiment, we construct v by Freeman–Durden decomposition [13] with other parameters being the same, i.e., $v = [P_s, P_d, P_v]^T$, where P_s, P_d, and P_v denote the surface scattering power, double bounce scattering power, and volume scattering power, respectively.
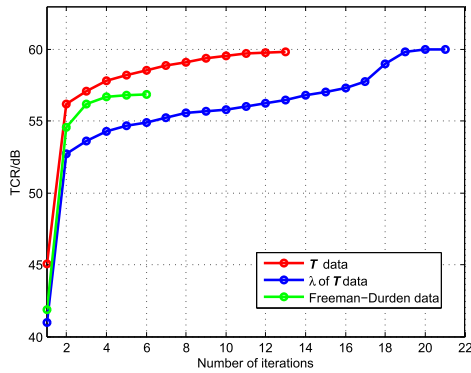
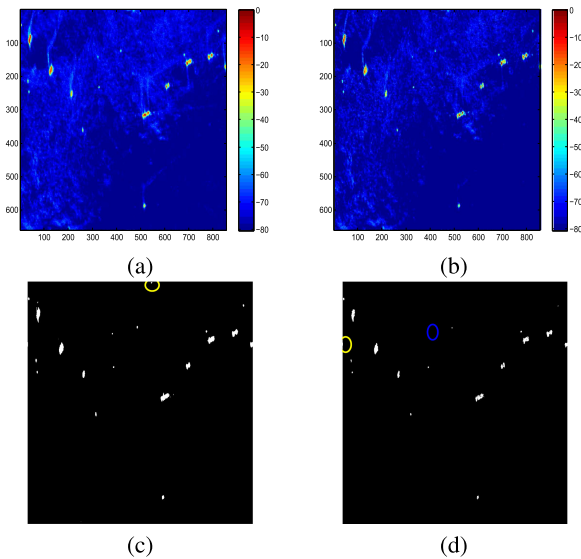Fig. 12.   TCR curve versus number of iterations for different polarization characteristics.

Fig. 13.   Enhanced and detected results for Patch D with different polarization characteristics. (a) Enhanced image with eigenvalue of $\boldsymbol{T}$. (b) Enhanced image with Freeman–Durden decomposition. (c) Detected result with eigenvalue. (d) Detected result with Freeman–Durden decomposition.

Fig. 12 depicts the TCR curve versus the number of iterations for different polarization characteristics. It is obvious that the proposed algorithm achieves the final TCR about 57 dB within six iterations for the eigenvalues of $\boldsymbol{T}$. When considering the Freeman–Durden polarization characteristics, the final TCR can reach about 60 dB within 21 iterations. Comparing with the original experiment using $\boldsymbol{T}$ data, different polarization characteristics perform differently at the enhancement stage. This phenomenon can be explained from the target enhancement optimization model, where the linear filter is used to enhance the targets, but the relationship among these polarization characteristics are nonlinear. Therefore, the optimal filter is unable to capture the inner relationship among them resulting in different enhancement results.

Different polarization characteristics influence the final detection results through the enhanced images. Fig. 13(a) and (b) shows the enhanced images associated with the eigenvalues of $\boldsymbol{T}$ and Freeman–Durden polarization characteristics, respectively. Fig. 13(c) and (d) shows the corresponding detection results with the upper bound of P_{fa} being 10^{-3}. One can see a false alarm

TABLE V
VALUES OF FOM AND P_r FOR DIFFERENT $\boldsymbol{v}$

Polarization characteristics	N_g	N_d	N_f	FoM	P_r
$\boldsymbol{T}$ matrix	18	18	1	1	0.95
Eigenvalue of $\boldsymbol{T}$	18	18	1	1	0.95
Freeman-Durden decomposition	18	17	1	0.94	0.89

in Fig. 13(c), which is consistent with the result in Fig. 7(d). However, they are essentially different since different enhanced images are used for detection. Compared with Fig. 13(c) or Fig. 7(d), Fig. 13(d) shows the differences brought by polarization characteristics, where a missed alarm as well as a false alarm can be seen in the figure.

Table V illustrates the values of FoM and P_r to give a further comparison on the effects caused by different polarization characteristics. The figures in Table V show that the characteristics extracted from Freeman–Durden decomposition perform slightly worse for Patch D.

Nevertheless, it is worth pointing out that the experimental results shown in this section only verify the fact that detection results are effected by the nonlinear transformation of polarization characteristics. Although the polarization characteristics constructed by $\boldsymbol{T}$ outperform the Freeman–Durden polarization characteristics, it is possible that this is no longer true for other PolSAR data. As to the problem that which one is the best polarization characteristic, it depends on practical situations.

VI. CONCLUSION

In this article, a distribution independent ship detector consisting of two stages is proposed for PolSAR images. In particular, ships are enhanced at the enhancement stage based on a nonconvex optimization model aiming at maximizing the TCR. A cyclic algorithm is devised to solve the nonconvex optimization problem, and the convergence as well as the computational complexities of the algorithm is analyzed. The detection stage is conducted on the enhanced images. Different from conventional CFAR detectors, thresholds of the proposed detector are calculated based on Markov inequality where only the clutter statistical moments are needed. Thus, the proposed detector is distribution independent with a bounded CFAR property. Finally, some experiments are carried out on the real Radarsat-2 and AirSAR data to demonstrate the effectiveness as well as the robustness of the proposed detector.

Although the proposed detector has the advantages mentioned earlier, experiments also show that the detection results are affected by the selection of polarization characteristics, since the linear filter cannot capture the nonlinear features hidden in the polarization characteristics. Our future research may involve in the adaptive nonlinear feature enhancement and corresponding ship detectors.

from the Center for Earth Observation and Digital Earth, Chinese Academy of Sciences.

REFERENCES

[1] G. Akbarizadeh, "A new statistical-based kurtosis wavelet energy feature for texture recognition of SAR images," *IEEE Trans. Geosci. Remote Sens.*, vol. 50, no. 11, pp. 4358–4368, Nov. 2012.

[2] Z. Tirandaz and G. Akbarizadeh, "A two-phase algorithm based on kurtosis curvelet energy and unsupervised spectral regression for segmentation of SAR images," *IEEE J. Sel. Topics Appl. Earth Observ. Remote Sens.*, vol. 9, no. 3, pp. 1244–1264, Mar. 2016.

[3] J.-S. Lee and E. Pottier, *Polarimetric Radar Imaging: From Basics to Applications*. Boca Raton, FL, USA: CRC Press, 2009.

[4] D. Xiang, T. Tang, Y. Ban, and Y. Su, "Man-made target detection from polarimetric SAR data via nonstationarity and asymmetry," *IEEE J. Sel. Topics Appl. Earth Observ. Remote Sens.*, vol. 9, no. 4, pp. 1459–1469, Apr. 2016.

[5] Z. Tirandaz, G. Akbarizadeh, and H. Kaabi, "PolSAR image segmentation based on feature extraction and data compression using weighted neighborhood filter bank and hidden Markov random field-expectation maximization," *Measurement*, vol. 153, 2020, Art. no. 107432.

[6] K. Ouchi, "Recent trend and advance of synthetic aperture radar with selected topics," *Remote Sens.*, vol. 5, no. 2, pp. 716–807, 2013.

[7] D. J. Crisp, "The state-of-the-art in ship detection in synthetic aperture radar imagery," Defence Sci. Technol. Org. Salisbury Info., Edinburgh, SA, Australia, Tech. Rep. DSTO-RR-0272, 2004.

[8] L. M. Novak, M. B. Sechtin, and M. J. Cardullo, "Studies of target detection algorithms that use polarimetric radar data," *IEEE Trans. Aerosp. Electron. Syst.*, vol. 25, no. 2, pp. 150–165, Mar. 1989.

[9] S. Brusch, S. Lehner, T. Fritz, M. Soccorsi, A. Soloviev, and B. van Schie, "Ship surveillance with TerraSAR-X," *IEEE Geosci. Remote Sens. Lett.*, vol. 49, no. 3, pp. 1092–1103, Mar. 2011.

[10] R. Chaney, M. Bud, and L. Novak, "On the performance of polarimetric target detection algorithms," *IEEE Aerosp. Electron. Syst. Mag.*, vol. 5, no. 11, pp. 10–15, Nov. 1990.

[11] L. M. Novak, M. C. Burl, and W. Irving, "Optimal polarimetric processing for enhanced target detection," *IEEE Trans. Aerosp. Electron. Syst.*, vol. 29, no. 1, pp. 234–244, Jan. 1993.

[12] W. L. Cameron, N. N. Youssef, and L. K. Leung, "Simulated polarimetric signatures of primitive geometrical shapes," *IEEE Trans. Geosci. Remote Sens.*, vol. 34, no. 3, pp. 793–803, May 1996.

[13] A. Freeman and S. L. Durden, "A three-component scattering model for polarimetric SAR data," *IEEE Trans. Geosci. Remote Sens.*, vol. 36, no. 3, pp. 963–973, May 1998.

[14] R. Ringrose and N. Harris, "Ship detection using polarimetric SAR data," in *Proc. SAR Workshop: CEOS Committee Earth Observ. Satell.*, 2000, vol. 450, Art. no. 687.

[15] A. Marino, "A notch filter for ship detection with polarimetric SAR data," *IEEE J. Sel. Topics Appl. Earth Observ. Remote Sens.*, vol. 6, no. 3, pp. 1219–1232, Jun. 2013.

[16] A. Marino and I. Hajnsek, "Statistical tests for a ship detector based on the polarimetric notch filter," *IEEE Trans. Geosci. Remote Sens.*, vol. 53, no. 8, pp. 4578–4595, Aug. 2015.

[17] T. Zhang, Z. Yang, and H. Xiong, "PolSAR ship detection based on the polarimetric covariance difference matrix," *IEEE J. Sel. Topics Appl. Earth Observ. Remote Sens.*, vol. 10, no. 7, pp. 3348–3359, Jul. 2017.

[18] T. Zhang, L. Jiang, D. Xiang, Y. Ban, L. Pei, and H. Xiong, "Ship detection from PolSAR imagery using the ambiguity removal polarimetric notch filter," *ISPRS J. Photogramm. Remote Sens.*, vol. 157, pp. 41–58, 2019.

[19] H. Lin, H. Wang, J. Wang, J. Yin, and J. Yang, "A novel ship detection method via generalized polarization relative entropy for PolSAR images," *IEEE Geosci. Remote Sens. Lett.*, 2020, pp. 1–5, doi: 10.1109/LGRS.2020.3019196.

[20] G. Gao and G. Shi, "CFAR ship detection in nonhomogeneous sea clutter using polarimetric SAR data based on the notch filter," *IEEE Trans. Geosci. Remote Sens.*, vol. 55, no. 8, pp. 4811–4824, Aug. 2017.

[21] X.-C. Cui, Y. Su, and S.-W. Chen, "A saliency detector for polarimetric SAR ship detection using similarity test," *IEEE J. Sel. Topics Appl. Earth Observ. Remote Sens.*, vol. 12, no. 9, pp. 3423–3433, Sep. 2019.

[22] C. P. Schwegmann, W. Kleynhans, and B. P. Salmon, "Manifold adaptation for constant false alarm rate ship detection in South African oceans," *IEEE J. Sel. Topics Appl. Earth Observ. Remote Sens.*, vol. 8, no. 7, pp. 3329–3337, Jul. 2015.

[23] F. C. Robey, D. R. Fuhrmann, E. J. Kelly, and R. Nitzberg, "A CFAR adaptive matched filter detector," *IEEE Trans. Aerosp. Electron. Syst.*, vol. 28, no. 1, pp. 208–216, Jan. 1992.

[24] J. Schou, H. Skriver, A. A. Nielsen, and K. Conradsen, "CFAR edge detector for polarimetric SAR images," *IEEE Trans. Geosci. Remote Sens.*, vol. 41, no. 1, pp. 20–32, Jan. 2003.

[25] J. Chen, Y. Chen, and J. Yang, "Ship detection using polarization cross-entropy," *IEEE Geosci. Remote Sens. Lett.*, vol. 6, no. 4, pp. 723–727, Oct. 2009.

[26] T. Li, Z. Liu, R. Xie, and L. Ran, "An improved superpixel-level CFAR detection method for ship targets in high-resolution SAR images," *IEEE J. Sel. Topics Appl. Earth Observ. Remote Sens.*, vol. 11, no. 1, pp. 184–194, Oct. 2017.

[27] W. Fan, F. Zhou, M. Tao, X. Bai, X. Shi, and H. Xu, "An automatic ship detection method for PolSAR data based on K-Wishart distribution," *IEEE J. Sel. Topics Appl. Earth Observ. Remote Sens.*, vol. 10, no. 6, pp. 2725–2737, Jun. 2017.

[28] P. Iervolino and R. Guida, "A novel ship detector based on the generalized-likelihood ratio test for SAR imagery," *IEEE J. Sel. Topics Appl. Earth Observ. Remote Sens.*, vol. 10, no. 8, pp. 3616–3630, Aug. 2017.

[29] O. Pappas, A. Achim, and D. Bull, "Superpixel-level CFAR detectors for ship detection in SAR imagery," *IEEE Geosci. Remote Sens. Lett.*, vol. 15, no. 9, pp. 1397–1401, Sep. 2018.

[30] S. Song, B. Xu, Z. Li, and J. Yang, "Ship detection in SAR imagery via variational Bayesian inference," *IEEE Geosci. Remote Sens. Lett.*, vol. 13, no. 3, pp. 319–323, Mar. 2016.

[31] Y. Wang and H. Liu, "PolSAR ship detection based on superpixel-level scattering mechanism distribution features," *IEEE Geosci. Remote Sens. Lett.*, vol. 12, no. 8, pp. 1780–1784, Aug. 2015.

[32] M. Rahmani and G. Akbarizadeh, "Unsupervised feature learning based on sparse coding and spectral clustering for segmentation of synthetic aperture radar images," *IET Comput. Vis.*, vol. 9, no. 5, pp. 629–638, 2015.

[33] F. Sharifzadeh, G. Akbarizadeh, and Y. S. Kavian, "Ship classification in SAR images using a new hybrid CNN-MLP classifier," *J. Indian Soc. Remote Sens.*, vol. 47, no. 4, pp. 551–562, 2019.

[34] Y. Li *et al.*, "Ship recognition from chaff clouds with sophisticated polarimetric decomposition," *Remote Sens.*, vol. 12, no. 11, 2020, Art. no. 1813.

[35] C. Liu, "Effects of target motion on polarimetric SAR images," *Can. J. Remote Sens.*, vol. 32, no. 2, pp. 51–56, 2006.

[36] S. R. Cloude and E. Pottier, "A review of target decomposition theorems in radar polarimetry," *IEEE Trans. Geosci. Remote Sens.*, vol. 34, no. 2, pp. 498–518, Mar. 1996.

[37] S. R. Cloude and E. Pottier, "An entropy based classification scheme for land applications of polarimetric SAR," *IEEE Trans. Geosci. Remote Sens.*, vol. 35, no. 1, pp. 68–78, Jan. 1997.

[38] S. M. Kay, *Fundamentals of Statistical Signal Processing*. Upper Saddle River, NJ, USA: Prentice-Hall, 1993.

[39] M. A. Richards, *Fundamentals of Radar Signal Processing*. New York, NY, USA: McGraw-Hill, 2005.

[40] Z. Lin and Z. Bai, *Probability Inequalities*. New York, NY, USA: Springer, 2011.

[41] Y. Nesterov, *Introductory Lectures on Convex Optimization: A Basic Course*. New York, NY, USA: Springer, 2013.

[42] S. Boyd, S. P. Boyd, and L. Vandenberghe, *Convex Optimization*. Cambridge, U.K.: Cambridge Univ. Press, 2004.

[43] F. Dufrenois and J. C. Noyer, "Formulating robust linear regression estimation as a one-class LDA criterion: Discriminative hat matrix," *IEEE Trans. Neural Netw. Learn. Syst.*, vol. 24, no. 2, pp. 262–273, Feb. 2013.

[44] F. Dufrenois, "A one-class kernel fisher criterion for outlier detection," *IEEE Trans. Neural Netw. Learn. Syst.*, vol. 26, no. 5, pp. 982–994, May 2015.

Zhou Xu was born in Yiyang, China, in 1990. He received the B.S. and M.S. degrees in electrical and electronic engineering from the Naval Aeronautical University, Yantai, China, in 2012 and 2014, respectively. He is currently working toward the Ph.D. degree in information and communication engineering with the College of Electronic Science and Engineering, National University of Defense Technology, Changsha, China.

Since 2016, he has been a Lecture with the College of Electronic Countermeasure, National University of Defense Technology, Hefei, China. His current research interests mainly include multichannel radar signal processing, convex optimization, and game theory on signal processing.

Chongyi Fan received the B.Eng. degree in electrical and electronic engineering and the Ph.D. degree in information and communication engineering from the National University of Defense Technology (NUDT), Changsha, China, in 2006 and 2012, respectively.

She is currently an Associate Professor with the College of Electronic Science and Engineering, NUDT. She teaches the courses of array signal processing, introduction of new concept radar, and signal and system. Her recent research interests include convex optimization, MIMO radar, and array signal processing.

Jian Wang received the B.S., M.S., and Ph.D. degrees in information and communication engineering from the National University of Defense Technology, Changsha, China, in 2003, 2004, and 2009, respectively.

He is currently a Lecturer with the College of Electronic Science and Engineering, National University of Defense Technology. His research interests include ground surveillance radar, target tracking, SAR image formation, and SAR interferometry.

Xiaotao Huang (Senior Member, IEEE) received the B.S. and Ph.D. degrees in information and communication engineering from the National University of Defense Technology, Changsha, China, in 1990 and 1999, respectively.

He is currently a Professor with the National University of Defense Technology. His fields of interest include radar theory, signal processing, and radio frequency signal suppression.

Shuiying Cheng received the M.S. and Ph.D. degrees in electronic and information engineering from Electronic Engineering Institute, Hefei, China, in 2000 and 2006, respectively.

He is currently an Associate Professor with the College of Electronic Countermeasure, National University of Defense Technology, Hefei, China. His research interests include radar signal processing and radar target recognition.